Poly(vinylidene fluoride)-Stabilized Black γ-Phase CsPbI3Perovskite for High-Performance Piezoelectric Nanogenerators

W. Zhu, A.A. Khan, M.M. Rana, R. Gautheron-Bernard, N.R. Tanguy, N. Yan, Pascal Turban, S. Ababou-Girard, D. Ban

ACS OMEGA

http://pubs.acs.org/journal/acsodf

Article

Poly(vinylidene fluoride)-Stabilized Black γ-Phase $CsPbI_3$ Perovskite for High-Performance Piezoelectric Nanogenerators

Weiguang Zhu, Asif Abdullah Khan, Md Masud Rana, Rozenn Gautheron-Bernard, Nicolas R. Tanguy, Ning Yan, Pascal Turban, Soraya Ababou-Girard, and Dayan Ban*

Cite This: *ACS Omega* 2022, 7, 10559−10567

Read Online

ACCESS | Metrics & More | Article Recommendations | Supporting Information

ABSTRACT: Halide perovskite materials have been recently recognized as promising materials for piezoelectric nanogenerators (PENGs) due to their potentially strong ferroelectricity and piezoelectricity. Here, we report a new method using a poly(vinylidene fluoride) (PVDF) polymer to achieve excellent long-term stable black γ-phase $CsPbI_3$ and explore the piezoelectric performance on a $CsPbI_3$@PVDF composite film. The PVDF-stabilized black-phase $CsPbI_3$ perovskite composite film can be stable under ambient conditions for more than 60 days and over 24 h while heated at 80 °C. Piezoresponse force spectroscopy measurements revealed that the black $CsPbI_3$/PVDF composite contains well-developed ferroelectric properties with a high piezoelectric charge coefficient (d_{33}) of 28.4 pm/V. The black phase of the $CsPbI_3$-based PVDF composite exhibited 2 times higher performance than the yellow phase of the $CsPbI_3$-based composite. A layer-by-layer stacking method was adopted to tune the thickness of the composite film. A five-layer black-phase $CsPbI_3$@PVDF composite PENG exhibited a voltage output of 26 V and a current density of 1.1 $\mu A/cm^2$. The output power can reach a peak value of 25 μW. Moreover, the PENG can be utilized to charge capacitors through a bridge rectifier and display good durability without degradation for over 14 000 cyclic tests. These results reveal the feasibility of the all-inorganic perovskite for the design and development of high-performance piezoelectric nanogenerators.

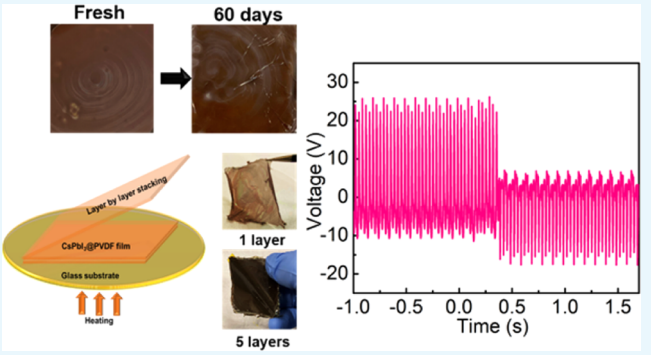

INTRODUCTION

The piezoelectric effect is considered as a promising solution to remit the energy crisis. Thus, piezoelectric nanogenerators (PENGs) have become a hot topic of research in terms of their potential to convert irregular mechanical energy to electric energy.[1] Various materials have been extensively adopted as piezoelectric materials for mechanical energy harvesting, such as ZnO,[2,3] GaN,[4] and a number of piezoelectric ceramics, including $BaTiO_3$[5] and lead zirconium titanate (PZT).[6,7] However, the growth and fabrication of these ceramic materials typically involve a very complex and cost-intensive process.[5] In addition, the brittle nature of the ceramics makes them fragile under mechanical force.[5,8] Therefore, it is vital to develop new materials that are easy to be fabricated and possess good performance for PENGs.

Recently, lead halide perovskites have been extensively investigated in the area of optoelectronic devices due to their excellent absorption coefficient, long diffusion length, high photoluminescence quantum efficiency, and superior electrical properties.[9−12] In addition, the spontaneous polarization of the organic−inorganic lead halide perovskites can be ascribed to the permanent dipoles provided by the molecular cations; in this case, it plays a key role in ferroelectricity.[13−15] Therefore, piezoelectric energy harvesting applications beyond photovoltaic solar cells have been explored. For instance, the $CH_3NH_3PbI_3$ perovskite has been reported with excellent piezoelectric properties, exhibiting an output voltage of 2.7 V and a current density of 140 nA/cm^2.[16] To improve the performance, the composite-based perovskites have been fabricated with perovskite nanoparticles embedded in polymers such as poly(dimethylsiloxane) (PDMS) and poly(vinylidene fluoride) (PVDF).[17−20] In comparison to the organic−inorganic halide perovskites, the all-inorganic counterparts are more stable in terms of moisture and heat.[21] Thus, $CsPbBr_3$ has been explored as a piezoelectric material with an excellent output voltage of ∼16.4 V and an output current of ∼604 nA for the 260 nm thick film.[22] The polymer-based $CsPbBr_3$ composites have also been investigated recently and shown improved performance.[23−25] However, there has been no report

Received: January 6, 2022
Accepted: March 4, 2022
Published: March 15, 2022

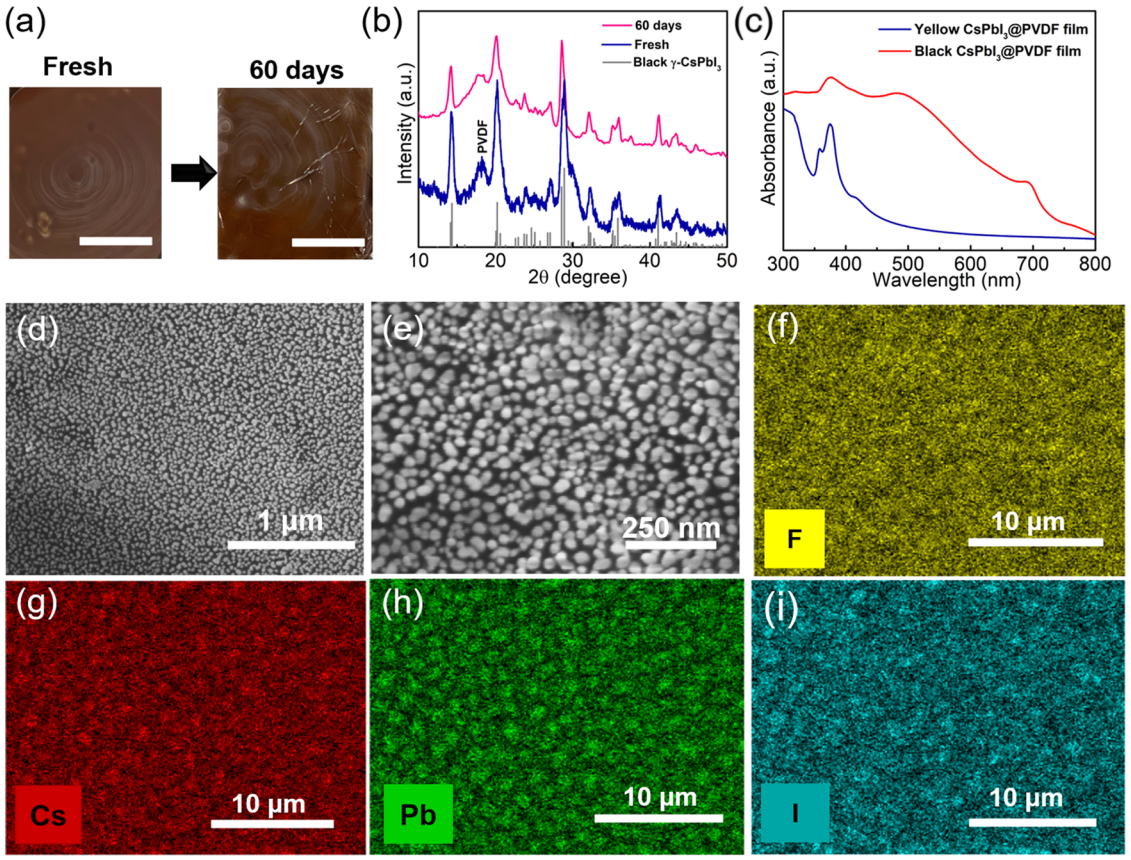

Figure 1. (a) Optical images of the prepared black-phase $CsPbI_3$@PVDF film and aging for 60 days at ambient conditions. Scale bar: 1 cm. (b) X-ray diffraction (XRD) spectrum of the black-phase $CsPbI_3$@PVDF film. The gray lines are the calculated black γ-phase $CsPbI_3$. (c) Ultraviolet−visible (UV−vis) absorption spectra of the prepared yellow and black $CsPbI_3$@PVDF films. (d, e) Scanning electron microscopic (SEM) images of the black-phase 20 wt % $CsPbI_3$@PVDF film. (f−i) Corresponding elemental mapping images of F, Cs, Pb, and I in Figure S4b of the black-phase 30 wt % $CsPbI_3$@PVDF film.

on the piezoelectric energy harvesting performance on the all-inorganic perovskite ($CsPbI_3$). Since the Cs^+ cation is small and near the lower limit for lead iodide perovskite formation, the black perovskite phase of $CsPbI_3$ can typically be stable at temperatures above 300 °C.[26] As temperature decreases to room temperature, $CsPbI_3$ suffers from thermodynamical phase transition to the yellow non-perovskite orthorhombic phase.[26,27] Although in a recent study it is found that the black perovskite phase of $CsPbI_3$ with an orthorhombic structure (γ-phase) can be obtained at room temperature through rapid quenching, the black phase is still not stable and degraded into a yellow-phase material while exposed to moisture.[28] Limited methods have been developed to sustain the perovskite phase of $CsPbI_3$ at room temperature.[29−32] For instance, Li et al.[29] have reported that poly(vinylpyrrolidone) (PVP) induces surface passivation on the surface of $CsPbI_3$ perovskite. The acylamino groups of PVP lead to electron cloud density enhancement on the surface of $CsPbI_3$, thus lowering surface energy and leading to a stable cubic α-phase $CsPbI_3$ at room temperature.

In this study, we present a simple but robust route of PVDF-passivated $CsPbI_3$ to stabilize the black γ-phase of $CsPbI_3$ perovskite and fabricate the $CsPbI_3$@PVDF composite for piezoelectric nanogenerators. The PVDF-stabilized black-phase $CsPbI_3$ perovskite composite film can be stable under ambient conditions for more than 60 days and over 24 h while heated at 80 °C. The PFM measurements of the black $CsPbI_3$/PVDF composite display well-developed ferroelectric properties with a high piezoelectric coefficient of 28.4 pm/V. A layer-by-layer stacking method was developed to fabricate $CsPbI_3$@PVDF composite films with a tunable film thickness. The yellow phase and black phase of the $CsPbI_3$-based composite films on piezoelectric performance were also compared. The black-phase $CsPbI_3$-based PVDF composite displays more than 2 times higher voltage and current output. By increasing the film thickness, the voltage output and current density of the black-phase $CsPbI_3$@PVDF-based PENG with five-layer stacking are obtained at a value of 26 V and 1.1 $\mu A/cm^2$, respectively, which is more than 6 times higher for voltage and 2 times higher for current output of the two-layer stacked composite PENG. The energy generated by the PENG can be used to charge capacitors. Also, the PENG can generate peak power at 25 μW. All of these results show that the all-inorganic perovskite has great potential in high-performance piezoelectric energy harvesting applications.

RESULTS AND DISCUSSION

The $CsPbI_3$@PVDF composite films were prepared via a simple and highly reproducible spin-coating process. Details of the preparation process are outlined in the Experimental Methods section. Typically, $CsPbI_3$/PVDF solution was spin-coated on a glass substrate. At different annealing temperatures, the phases of $CsPbI_3$ within the composite could be tuned. As shown in Figure S1, a pure yellow color $CsPbI_3$@PVDF composite film

https://doi.org/10.1021/acsomega.2c00091
ACS Omega 2022, 7, 10559−10567

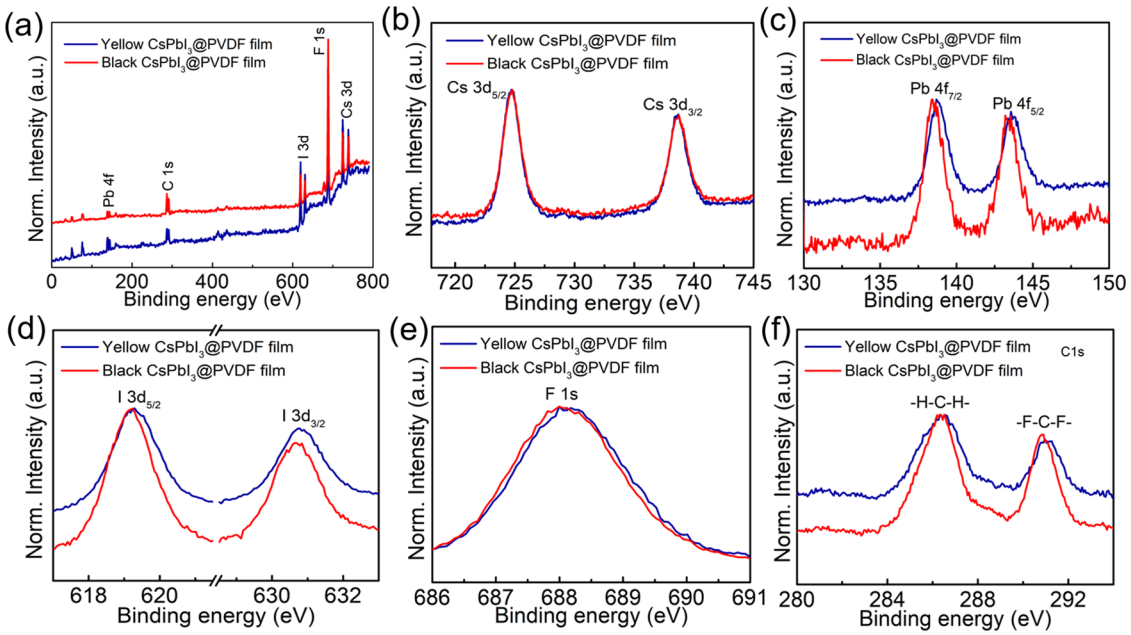

Figure 2. (a) X-ray photoelectron spectroscopy (XPS) survey spectra of yellow and black color $CsPbI_3$@PVDF composite films. The high-resolution XPS spectra of (b) Cs 3d, (c) Pb 4f, (d) I 3d, (e) F 1s, and (f) C 1s.

was obtained at 50 °C. By increasing the temperature to 70 °C, a partially brown area could be identified in the composite film, indicating that part of $CsPbI_3$ formed as black phase. Further increasing the temperature above 130 °C, the color of the $CsPbI_3$@PVDF composite film turned to a pure dark-brown or black color (depending on the thickness), suggesting the formation of the pure black-phase $CsPbI_3$. The photograph in Figure 1a shows that the black-phase $CsPbI_3$@PVDF composite film can be sustained at room temperature and remains stable for more than 60 days. Under ambient conditions and at 80 °C, it also displayed excellent thermal stability without obvious color changes for over 24 h (Figure S2), indicating that the black phase of $CsPbI_3$ can be well-sustained within PVDF under different conditions. The X-ray diffraction (XRD) patterns of $CsPbI_3$@PVDF composite films presented differences in the crystal structures of films obtained at different temperatures. At a low temperature (50 °C), a yellow color $CsPbI_3$@PVDF film was obtained and displayed the orthorhombic yellow δ-$CsPbI_3$ phase, as shown in Figure S3. As the temperature increased to 70 °C, the interaction between PVDF and $CsPbI_3$ increased, new XRD peaks started to appear within the obtained composite, which could be assigned to the black γ-phase of $CsPbI_3$. In addition, the peak at 20.2° could be assigned to the β-phase of PVDF. By further increasing the temperature, the film obtained at 180 °C exhibited the black γ-$CsPbI_3$ perovskite with an orthorhombic crystal structure, as shown in Figures 1b and S3. The peaks at 17.7, 18.2, and 26.2° could also be identified, which could be ascribed to α-phase PVDF.[33] It was noticed that the (110) peak of α-phase PVDF could not be resolved as it was positioned close to the (112) peak of the black γ-$CsPbI_3$ perovskite at 20.2°. In addition, the XRD pattern obtained after 60 days matches well with that of the freshly prepared sample, indicating the good stability of the black $CsPbI_3$ perovskite in PVDF (Figure 1b). Figure 1c presents the ultraviolet−visible (UV−vis) absorption spectra of the $CsPbI_3$@PVDF film obtained at different temperatures. The yellow $CsPbI_3$@PVDF film exhibited a limited visible-light-absorption range of less than 450 nm. In contrast, the black $CsPbI_3$@PVDF film showed an absorption edge above 700 nm, which is consistent with the results from the literature.[28,30] This indicates the successful formation of the black-phase $CsPbI_3$ within the composite film.

The surface morphology of the black-phase 20 wt % $CsPbI_3$@PVDF film is shown in Figure 1d. It exhibits $CsPbI_3$ particles uniformly embedded within PVDF. A closer observation of $CsPbI_3$ particles under high magnifications reveals small $CsPbI_3$ nanocrystals with a size of ∼50 nm, as shown in Figure 1e. As the concentration increased, the obtained 30 wt % $CsPbI_3$@PVDF film turned from a dark-brown color to a black color (Figure S4a) and exhibited larger crystals with sizes over 500 nm (Figure S4b). Although due to the fast $CsPbI_3$ precipitation (within a few seconds) when heated at 180 °C, a few crystal agglomerates on the film surface were observed; there could still be a very thin PVDF film on the crystal surface and passivate the perovskite material, stabilizing the black γ-phase $CsPbI_3$. It should be noted that the films prepared with different concentrations of $CsPbI_3$ are all very stable in air, without obvious degradation for over 6 months (Figure S5). Figure 1f−i shows the EDS elemental mappings of F, Cs, Pb, and I; it demonstrates that $CsPbI_3$ crystals were dispersed homogeneously in the PVDF polymer and formed the homogeneous $CsPbI_3$-PVDF matrix.

To gain more insights into the PVDF stabilization mechanism on the orthorhombic black-phase $CsPbI_3$, we conducted X-ray photoelectron spectroscopy (XPS) measurements on both yellow and black $CsPbI_3$@PVDF films. The full XPS spectra are shown in Figure 2a. XPS analyses of the high-resolution spectra involving Cs 3d, Pb 4f, I 3d, F 1s, and C 1s were then performed to further clarify their electronic states. Figure 2b shows the typical Cs 3d spectra with no evident peak shifting, in which the strong peaks at 724.83 and 738.68 eV corresponding to Cs $3d_{5/2}$ and Cs $3d_{3/2}$, respectively (Figure 2b). As shown in Figure 2c, the Pb 4f spectrum for the yellow $CsPbI_3$@PVDF film was recorded with two contributions $4f_{5/2}$ and $4f_{7/2}$ located at 138.68 and 143.56 eV, respectively. As for the black $CsPbI_3$@PVDF film, the Pb 4f spectrum shifted to a lower binding energy. Similarly, the two I 3d peaks, corresponding to $3d_{5/2}$ and $3d_{3/2}$,

https://doi.org/10.1021/acsomega.2c00091
ACS Omega 2022, 7, 10559−10567

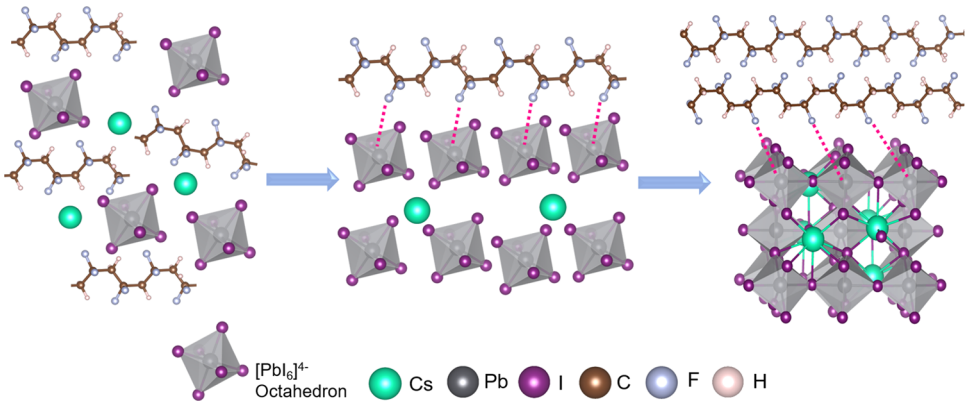

Figure 3. Schematic illustration of the crystal growth and the chemical bonding between $CsPbI_3$ and PVDF.

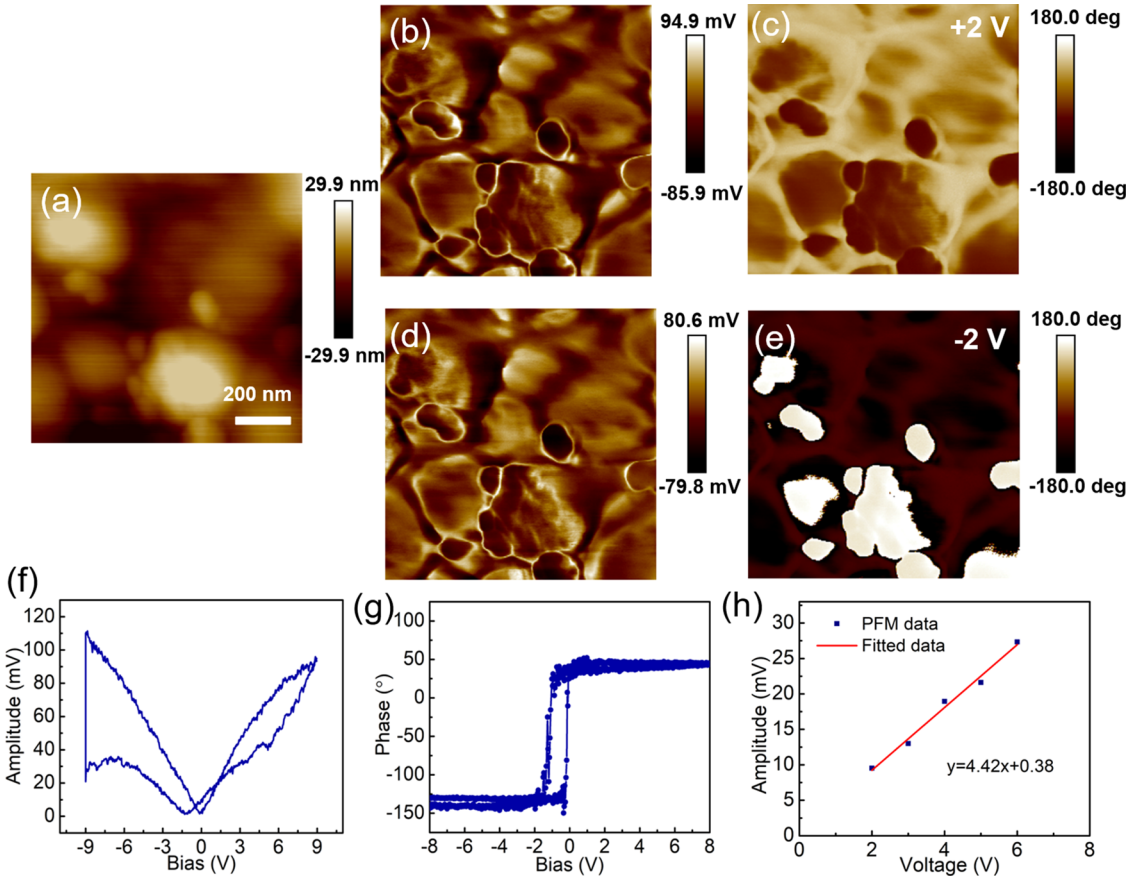

Figure 4. (a) Topography image of a selected region of the black $CsPbI_3$/PVDF composite. Piezoelectric force microscopy (PFM) measurements of the polarization reversal process. (b) Amplitude and (c) phase images at +2 V DC voltage bias; (d) amplitude and (e) phase images at −2 V DC voltage bias. (f) Amplitude loop, (g) phase hysteresis loop, and (h) PFM amplitude versus the AC voltage of the black $CsPbI_3$/PVDF composite at 0 V DC bias.

of the black $CsPbI_3$@PVDF film were located at lower binding energies compared with those of the yellow composite film, as shown in Figure 2d. This indicates the modified chemical environment of the $[PbI_6]^{4-}$ anion and the weaker Pb−I interaction during the formation of the black-phase $CsPbI_3$ crystals in PVDF. As shown in Figure 2e, the F 1s spectrum originating from the PVDF polymer exhibited a lower binding energy shifting as well for the black $CsPbI_3$@PVDF film. In addition, the C 1s spectrum in Figure 2f shows two peaks corresponding to −H−C−H− and −F−C−F−. The −F−C−F− from the black $CsPbI_3$@PVDF film showed a lower binding energy than that of the yellow composite film, confirming that the interaction between $CsPbI_3$ and PVDF leads to the stabilization of the black-phase $CsPbI_3$ perovskite. In the FTIR measurements (Figure S6), compared to the pure PVDF, the slight shifts of $-CF_2$ and the $-CF_2$ symmetrical stretching mode of the black $CsPbI_3$@PVDF film also indicate the interaction between PVDF and $CsPbI_3$.

Based on the above experimental facts, the schematic illustration in Figure 3 summarizes the potential role of PVDF in the crystal growth and phase stabilization of $CsPbI_3$. It is known that the lone pairs from fluorine atoms in the molecule of

https://doi.org/10.1021/acsomega.2c00091
ACS Omega 2022, 7, 10559−10567

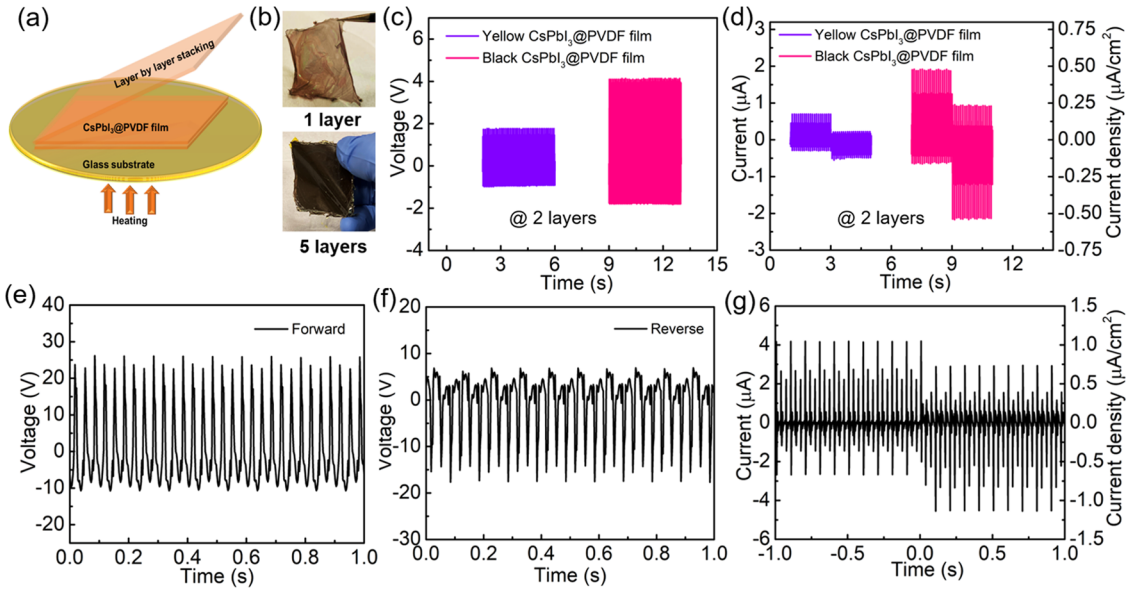

Figure 5. (a) Schematic of fabrication of $CsPbI_3$@PVDF composite films with different thicknesses through layer-by-layer stacking. (b) Optical images of one-layer and five-layer $CsPbI_3$@PVDF films. Comparison of the output of (c) open-circuit voltage and (d) current between two-layer yellow and black $CsPbI_3$@PVDF films. (e) Piezoelectric output voltage of the five-layer black $CsPbI_3$@PVDF film-based PENG in the forward connection. (f) Piezoelectric output voltage of the PENG in the reverse connection. (g) Piezoelectric output current of the PENG with obvious current switching.

PVDF determine the conformations of the crystalline PVDF. Each fluorine atom possesses three lone pairs, which offer a large number of coordination centers. At the initial stage, PVDF molecules attract the cations from $CsPbI_3$ precursors due to the long backbone chain ($-CH_2-CF_2-$) and the electronegative $-CF_2-$ group structure. Compared with the Cs cation, Pb^{2+} has a higher ionic potential,[34] which tends to be more easily attracted to the fluorine surface and forms a bond. Then, the positive and negative ions of $CsPbI_3$ assemble and bond to form the black-phase $CsPbI_3$ perovskite structure around the $-CF_2-$ groups. With increasing time, the long-chain PVDF molecule anchored at the surface of $CsPbI_3$ crystals can further protect the material from air and moisture, increasing the stability of the black-phase $CsPbI_3$ perovskite. Therefore, the black-phase $CsPbI_3$ perovskite can still be maintained after 60 days at ambient conditions for the PVDF chemically functionalized $CsPbI_3$. While we were preparing the revised manuscript, we noticed a new publication of a yellow δ-phase $CsPbI_3$/PVDF-based nanogenerator.[35] Based on their first-principles density functional theory (DFT) calculations, it is found that the interaction between $CsPbI_3$ and PVDF, through the bonding of the F of PVDF with the Cs and Pb within $CsPbI_3$, could enhance the polarization and decrease the band gap of $CsPbI_3$. Although the authors did not observe the transformation of the yellow-phase $CsPbI_3$ to the black phase through the interaction between PVDF and $CsPbI_3$, this still serves as a strong support for our experimental observation that bondings are formed between PVDF and the $CsPbI_3$ perovskite. The extra strain induced by PVDF on the $CsPbI_3$ perovskite prevents its structural change to the yellow δ-phase, leading to the stabilization of the black γ-phase PVDF.

Furthermore, the domain structure and polarization switching behavior of the $CsPbI_3$/PVDF composite were investigated using piezoresponse force microscopy (PFM). Figure 4a shows a representative topography image of the black $CsPbI_3$/PVDF composite with a square of $1 \times 1\ \mu m^2$. The small grain size in the range of 100−200 nm in the topography image can be attributed to the compact and uniform distribution of black-phase $CsPbI_3$ nanoparticles within the PVDF matrix. The amplitude image under a DC voltage bias of 2 V between the tip and the sample is shown in Figure 4b. The PFM signal variation exhibited a well-correlated relation with the grain boundaries, as shown in the topography image (Figure 4a). In addition, the domains coexisting in the same grain also showed distinct amplitude responses (Figure 4b), ruling out the possible artifacts due to grain boundaries or sharp edges. The phase variation image is shown in Figure 4c, showing many downpolarized domains under a 2 V DC bias. As the DC bias was reversed to a negative voltage, the amplitude of the domains did not show a very obvious change (Figure 4d). However, the phase image shows that the domains appeared to be reversed by ∼180° at −2 V DC bias, indicating an upward polarization. Figure 4f,g show the amplitude loop and hysteresis loop in the phase angle, with a bias voltage of ±9 V, respectively. The amplitude loop exhibits a characteristic butterfly shape, and the phase angle loop shows a 180° difference, which is consistent with the phase images obtained at reversed DC biases. In addition, amplitude loops and phase hysteresis loops were measured at multiple locations, displaying similar results (Figure S7). The results confirm the presence of ferroelectricity-like behavior in the black $CsPbI_3$/PVDF composite thin film. As shown in Figure S8, several characteristic peaks at 613, 763, 976, and 1149 cm^{-1} could be ascribed to the nonpolar α-phase PVDF, which is consistent with the results from the literature.[33,36] In addition, based on our XRD results, α-phase PVDF could be identified within the black $CsPbI_3$@PVDF composite as discussed above (Figure S3). It indicates that the black γ-phase of $CsPbI_3$ stabilized by PVDF exhibits a ferroelectric nature. Since the amplitude image is proportional to the magnitude of the piezoelectric coefficient (d_{33}), the d_{33} can be calculated by the equation[37] $d_{33} = \frac{A}{U} = \frac{V\delta}{U}$, where A is the amplitude, V is the vertical deflection signal of the cantilever (mV, 16 times gain), δ is the tip sensitivity (103 nm/V), and U is the amplitude of the AC voltage. Figure 4h shows the AC voltage versus piezoresponse of the black $CsPbI_3$/PVDF

https://doi.org/10.1021/acsomega.2c00091
ACS Omega 2022, 7, 10559−10567

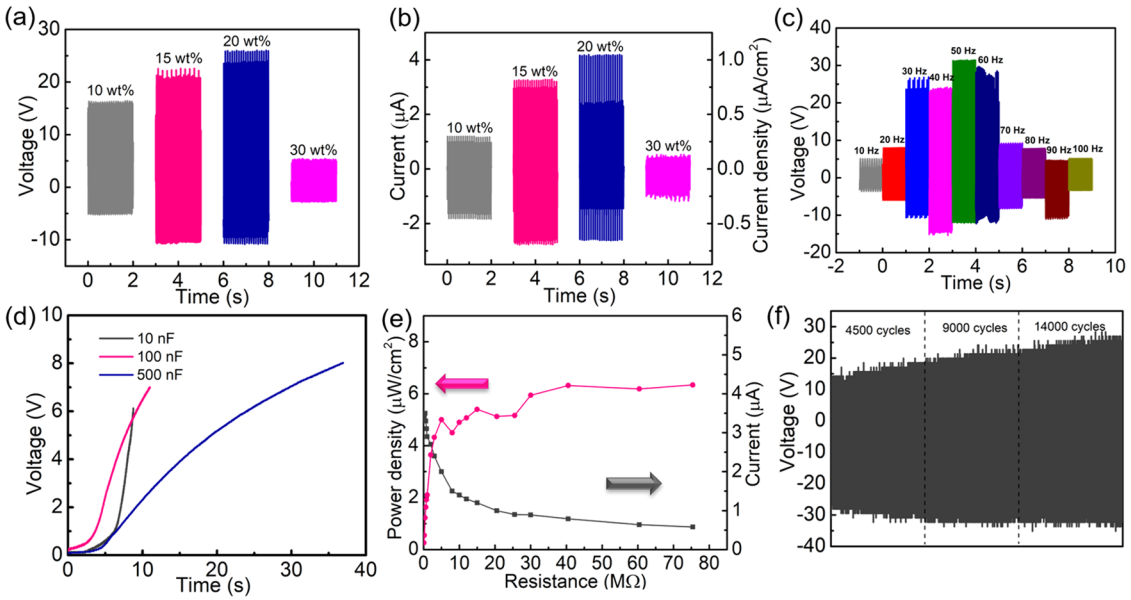

Figure 6. (a) Voltage output and (b) current output of the five-layer black-phase $CsPbI_3$@PVDF composite film with different mass ratios of $CsPbI_3$ in PVDF. (c) Output performance of the piezoelectric nanogenerator (five-layer black-phase 20 wt % $CsPbI_3$@PVDF) as a function of different frequencies. (d) Measured output voltage across the various commercial capacitors of 10, 100, and 500 nF charged by a PENG. (e) Current output and power density at various resistance loadings. (f) Stability of the PENG tested under a frequency of 30 Hz for 14 000 cycles.

composite. The slope was fitted with a linear function, and the value is shown in Figure 4h. The piezoelectric coefficient was estimated to be 28.4 pm/V, which is similar to the value of $BaTiO_3$ nanoparticles (28 pm/V)[38] and comparable to that of the $FAPbI_3$ nanoparticle.[17] The variation in the dielectric constant with frequency for the black $CsPbI_3$/PVDF composite was observed in the frequency range 1−100 kHz at room temperature (shown in Figure S9a). It is observed that the dielectric constant decreases as the frequency increases, which is a well-known behavior of dielectric materials.[39,40] The dielectric constant of the black $CsPbI_3$/PVDF composite was 17.6 at 1 kHz, which is higher than that of the pure PVDF.[41] The electric field-dependent leak current of the black $CsPbI_3$/PVDF composite is shown in Figure S9b. The leakage current is less than 10^{-6} A over the electrical field range of ±100 kV/cm. Therefore, the black $CsPbI_3$/PVDF composite films with high dielectric constant and low leakage current are beneficial for energy harvesting applications.

To explore the piezoelectric output performance, piezoelectric nanogenerators were fabricated. The thickness of the composite films can be well controlled through a layer-by-layer stacking method, as illustrated in Figure 5a. Figure 5b shows the optical image of a one-layer $CsPbI_3$@PVDF thin film with semitransparency. In the cross-section SEM image, the thickness was ∼1.5 μm, as shown in Figure S10a. However, the five-layer film showed a darker color and a flat surface with no obvious air bubbles, suggesting that the fabricated film has a good quality and interfacial contact. The cross-section SEM images of the five-layer film (Figure S10b) showed a compact film with a thickness of ∼10 μm. To explore the piezoelectric performance between the yellow-phase and the black-phase $CsPbI_3$, two-layer $CsPbI_3$@PVDF composite films with different $CsPbI_3$ phases were fabricated as PENGs. It can be clearly seen that the black-phase $CsPbI_3$@PVDF composite-based PENG exhibits more than 2 times higher output on the voltage and current density, as shown in Figure 5c,d. This suggests that the black-phase $CsPbI_3$-based PVDF composite exhibits better performance. To further increase the performance, five-layer black-phase $CsPbI_3$@PVDF composite film-based PENGs were fabricated. Under a 2.7 N applied force at a frequency of 30 Hz, the voltage output under a forward bias can reach a value of 26 V, which is much better than that of the two-layer black-phase-based PENG (4.1 V), as shown in Figure 5e. Switching-polarity tests were also carried out to verify the generated output signals originating from the piezoelectric phenomenon. A reverse connection was made, and an opposite output signal was measured, as shown in Figure 5f. It is obvious that the electric signals are reversible, indicating that the output signals are generated from the PENG strained by the electrodynamic shaker. In addition, a difference in the voltage peak values was observed, which could be attributed to the difference in the force in the process of applying and releasing force on the piezoelectric nanogenerator. Figure S11 shows the voltage and current output of the black $CsPbI_3$@PVDF-based nanogenerator at different applied forces. When the applied force decreased from 2.7 to 1.1 N, the piezoelectric outputs of voltage and current decreased gradually. When the applied force was lower than 1 N, the output voltage and current exhibited significant decreases, which indicates the lower sensitivity of the applied force as a force below 1 N. Figure 5g displays the current output with a peak current of 4.5 μA, corresponding to a 1.1 $\mu A/cm^2$. The switching output could also be observed while changing the connection, which confirms that the generated output is from the piezoelectric phenomenon.

To optimize the performance, the black-phase $CsPbI_3$@PVDF composite films with different $CsPbI_3$ mass ratios were also investigated. As shown in Figure 6a, for $CsPbI_3$ with mass ratios of 10, 15, 20, and 30 wt %, the voltage outputs of the device were 16, 22, 26, and 5.5 V, respectively, indicating that the PENG with $CsPbI_3$ with a mass ratio of 20 wt % exhibited the best output. As shown in Figure 6b, a similar trend was observed for current density, with mass ratios of 10, 15, 20, and 30 wt % exhibiting 0.45, 0.8, 1.1, and 0.28 μA, respectively. The frequency dependence was also investigated within a range from 10 to 100 Hz, as shown in Figure 6c. It is of great

https://doi.org/10.1021/acsomega.2c00091
ACS Omega 2022, 7, 10559−10567

importance to study the relationship between the output performance of the piezoelectric nanogenerator under different frequencies because the mechanical energy from the ambient environment can be varied significantly and irregularly.[42] The test was performed on the five-layer black-phase 20 wt % $CsPbI_3$ in PVDF composite-based PENG. As the frequency increased, the piezoelectric output increased, and the output voltage reached a peak value of 31 V at 50 Hz, as shown in Figure 6c. In addition, the voltage output can display high performance in a relatively large frequency range from 30 to 60 Hz without obvious degradation. On further increasing the frequency in the range of 70−100 Hz, the voltage output was much lower and decreased slightly with the increase in frequency. To demonstrate an example of the practical application of the $CsPbI_3$@PVDF composite-based PENG, the output signals generated by an electrodynamic shaker were directly used for charging capacitors, as shown in Figure 6d. The generated output was rectified through a full-wave bridge rectifier circuit. The capacitors can be gradually charged up with different rates depending on the capacitance. Higher capacitance results in a longer charging time of the capacitor. For a 100 nF capacitor, it only takes 10 s to reach 7 V, while 30 s is needed to charge a 500 nF capacitor to 7 V. Figure 6e shows the output power of the five-layer black-phase 20 wt % $CsPbI_3$@PVDF composite-based PENG as a function of load resistance. As the resistance increases, the output current gradually decreases. The peak output power was calculated to be 25 μW at a load of 40.5 MΩ, corresponding to a peak power density of 6.3 $\mu W/cm^2$. The cycle stability was also measured, as shown in Figure 6f. It was noticed that the output voltage has a tendency to increase with the increase of the number of cycles, which could be caused by the charge accumulation from the incomplete discharge during the cyclic charging and discharging processes. The charge accumulated in the previous process had not fully discharged, and the next cycle had already started, resulting in continuously increasing voltage output.[43] After 14 000 cycles, the black-phase $CsPbI_3$@PVDF composite-based PENG could still maintain a good output without a noticeable decrease, confirming the good stability and durability of the fabricated device.

CONCLUSIONS

We have described a novel approach to fabricate the black γ-phase $CsPbI_3$ perovskite using PVDF. The polymer not only works as a matrix to form the $CsPbI_3$@PVDF composite but also passivates the surface of $CsPbI_3$ through the interaction between the $-CF_2-$ structure and $CsPbI_3$. The obtained black-phase $CsPbI_3$@PVDF composite film was stable under ambient conditions for over 60 days and no obvious degradation under 80 °C for over 24 h. Piezoresponse force spectroscopy measurements suggest that the black $CsPbI_3$/PVDF composite contains well-developed ferroelectric properties with a high piezoelectric charge coefficient (d_{33}) of 28.4 pm/V. The piezoelectric performance between the yellow-phase and black-phase-based $CsPbI_3$@PVDF composite was also compared. The output signals of the black composite are more than 2 times higher than those from the yellow one. A layer-by-layer stacking method was adopted to fabricate composite films with a tunable thickness. The five-layer black-phase 20 wt % $CsPbI_3$@PVDF composite-based PENG can generate a voltage and current density output of 26 V and 1.1 $\mu A/cm^2$, respectively. The generated output signals from the nanogenerator can be used to charge capacitors. The output power can reach a peak value at 25 μW at a load of 40.5 MΩ. In addition, the fabricated PENG has excellent durability with no obvious degradation under 14 000 cyclic tests. This PVDF-stabilized $CsPbI_3$ method could be adopted as a new method for other functional applications. This simple, cost-effective solution process is feasible for the fabrication of large-scale high-performance all-inorganic perovskite composite-based piezoelectric nanogenerators with good stability and durability.

EXPERIMENTAL METHODS

Material Synthesis. *Synthesis of $CsPbI_3$ NPs.* Cesium iodide (CsI; 259 mg) and 462 mg of lead iodide (PbI_2) were dissolved in 25 mL of dimethylformamide (DMF) with 0.75 mL *of n*-octylamine (OTA) and 5 mL of oleic acid (OA). Then, the mixture was heated at 60 °C for 60 min while stirring. The mixture was dropped into 250 mL of toluene with vigorous stirring for 5 min. After centrifugation and purification, the $CsPbI_3$ nanocrystals were collected for further use.

Fabrications of $CsPbI_3$@PVDF Composite Films. $CsPbI_3$ NPs were homogeneously mixed with a PVDF solution (10 wt % in DMF) in different ratios of 10, 20, and 30 wt % and stirred at room temperature overnight. The as-mixed composite was spin-coated (500 rpm, 30 s) on a glass substrate and dried at different temperatures (50, 70, 130, and 180 °C) to control the final $CsPbI_3$ phases. The solid $CsPbI_3$@PVDF composite film was peeled off from the glass substrate for further characterization and device fabrication. The black-phase $CsPbI_3$@PVDF films were prepared at 180 °C for further characterization unless otherwise specified.

Device Fabrication. To tune the thickness of the $CsPbI_3$@PVDF composite film, multiple thin films were stacked on each other and annealed at 170 °C under vacuum for 5 min to eliminate air gaps. The composite films were polarized at room temperature with an electric field of ∼300 kV/cm for the black $CsPbI_3$@PVDF composite and 700 kV/cm for the yellow $CsPbI_3$@PVDF composite for 2 h. Then, the composite film was sandwiched between two patterned copper electrodes on the laminating pouches. The sandwiched structure of copper/$CsPbI_3$@PVDF/copper was pressed with a commercial thermal laminator to encapsulate the device. The thickness of the $CsPbI_3$@PVDF composite film was controlled by stacking different layers of thin films.

Measurements and Characterizations. The crystalline structures and phases of the thin films were characterized by X-ray diffraction (D8 Discover, Bruker) and Fourier transform infrared spectroscopy (Nicolet iS50, Thermo), respectively. Scanning electron microscopy (SEM) and energy-dispersive X-ray spectroscopy (EDS) were conducted by a field emission SEM (JSM 7200F). X-ray photoelectron spectroscopy (XPS) was performed with an Mg Kα ($h\nu$ = 1254.6 eV) X-ray source using a VSW HA100 photoelectron spectrometer. UV−vis spectra were obtained using a UV-2501PC (Shimadzu). Piezoelectric force microscopy measurements (Dimension Icon, Bruker) were taken in the contact and vertical mode with an AC voltage bias applied to the conductive AFM tip and the bottom electrode grounded. The piezoelectric nanogenerator performance was tested using an electrodynamic shaker (Lab Works Inc.). More details on the device measurements could be found in our previous reports.[19,44,45] The applied mass was 138 g at an acceleration of 2 G. The calculated force (F) was around 2.7 N based on the equation of $F = MA$. If not specified, all of the measurements were tested at a force of 2.7 N. By controlling the mass loading and the acceleration, the electromechanical response along with differ-

https://doi.org/10.1021/acsomega.2c00091
ACS Omega 2022, 7, 10559−10567

ent loadings could be analyzed. The voltage and current were measured with a digital oscilloscope (Tektronix 2004C) and a low-noise current preamplifier (model SR 570, Stanford Research System Inc.), respectively.

■ ASSOCIATED CONTENT

Supporting Information

The Supporting Information is available free of charge at https://pubs.acs.org/doi/10.1021/acsomega.2c00091.

Optical images and XRD patterns of $CsPbI_3$/PVDF composite films prepared at different temperatures, FTIR measurements of the composite films, SEM images of the black $CsPbI_3$/PVDF composite, piezoelectric nanogenerator performance of the black $CsPbI_3$/PVDF composite at different applied forces (PDF)

■ AUTHOR INFORMATION

Corresponding Author

Dayan Ban − *Waterloo Institute for Nanotechnology, University of Waterloo, Waterloo, Ontario N2L 3G1, Canada; Department of Electrical and Computer Engineering, University of Waterloo, Waterloo, Ontario N2L 3G1, Canada; School of Physics and Electronics, Henan University, Kaifeng 475001 Henan, P. R. China*; Email: dban@uwaterloo.ca

Authors

Weiguang Zhu − *Waterloo Institute for Nanotechnology, University of Waterloo, Waterloo, Ontario N2L 3G1, Canada;* orcid.org/0000-0003-0007-9284

Asif Abdullah Khan − *Waterloo Institute for Nanotechnology, University of Waterloo, Waterloo, Ontario N2L 3G1, Canada*

Md Masud Rana − *Waterloo Institute for Nanotechnology, University of Waterloo, Waterloo, Ontario N2L 3G1, Canada;* orcid.org/0000-0002-8026-9821

Rozenn Gautheron-Bernard − *Univ Rennes, CNRS, IPR (Institut de Physique de Rennes) - UMR 6251, F-35000 Rennes, France*

Nicolas R. Tanguy − *Department of Chemical Engineering and Applied Chemistry, University of Toronto, Toronto, Ontario M5S 3E5, Canada;* orcid.org/0000-0002-1205-5389

Ning Yan − *Department of Chemical Engineering and Applied Chemistry, University of Toronto, Toronto, Ontario M5S 3E5, Canada;* orcid.org/0000-0003-3371-1709

Pascal Turban − *Univ Rennes, CNRS, IPR (Institut de Physique de Rennes) - UMR 6251, F-35000 Rennes, France*

Soraya Ababou-Girard − *Univ Rennes, CNRS, IPR (Institut de Physique de Rennes) - UMR 6251, F-35000 Rennes, France*

Complete contact information is available at: https://pubs.acs.org/10.1021/acsomega.2c00091

Notes

The authors declare no competing financial interest.

The data that support the findings of this study are available from the corresponding author upon reasonable request.

■ ACKNOWLEDGMENTS

This work is supported by the Natural Science and Engineering Research Council of Canada, Ontario Centers of Excellence, and University of Waterloo.

■ REFERENCES

(1) Wang, Z. L.; Song, J. Piezoelectric Nanogenerators Based on Zinc Oxide Nanowire Arrays. *Science* **2006**, *312*, 242−246.

(2) Zhu, G.; Yang, R.; Wang, S.; Wang, Z. L. Flexible High-Output Nanogenerator Based on Lateral ZnO Nanowire Array. *Nano Lett.* **2010**, *10*, 3151−3155.

(3) Hu, Y.; Zhang, Y.; Xu, C.; Zhu, G.; Wang, Z. L. High-Output Nanogenerator by Rational Unipolar Assembly of Conical Nanowires and Its Application for Driving a Small Liquid Crystal Display. *Nano Lett.* **2010**, *10*, 5025−5031.

(4) Wang, C. H.; Liao, W. S.; Lin, Z. H.; Ku, N. J.; Li, Y. C.; Chen, Y. C.; Wang, Z. L.; Liu, C. P. Optimization of the Output Efficiency of GaN Nanowire Piezoelectric Nanogenerators by Tuning the Free Carrier Concentration. *Adv. Energy Mater.* **2014**, *4*, No. 1400392.

(5) Park, K. I.; Lee, M.; Liu, Y.; Moon, S.; Hwang, G. T.; Zhu, G.; Kim, J. E.; Kim, S. O.; Kim, D. K.; Wang, Z. L.; et al. Flexible Nanocomposite Generator Made of $BaTiO_3$ Nanoparticles and Graphitic Carbons. *Adv. Mater.* **2012**, *24*, 2999−3004.

(6) Xu, S.; Yeh, Y.-w.; Poirier, G.; McAlpine, M. C.; Register, R. A.; Yao, N. Flexible Piezoelectric PMN−Pt Nanowire-Based Nanocomposite and Device. *Nano Lett.* **2013**, *13*, 2393−2398.

(7) Xu, S.; Poirier, G.; Yao, N. PMN-Pt Nanowires with a Very High Piezoelectric Constant. *Nano Lett.* **2012**, *12*, 2238−2242.

(8) Huang, C.-T.; Song, J.; Lee, W.-F.; Ding, Y.; Gao, Z.; Hao, Y.; Chen, L.-J.; Wang, Z. L. GaN Nanowire Arrays for High-Output Nanogenerators. *J. Am. Chem. Soc.* **2010**, *132*, 4766−4771.

(9) Zhou, H.; Chen, Q.; Li, G.; Luo, S.; Song, T.-b.; Duan, H.-S.; Hong, Z.; You, J.; Liu, Y.; Yang, Y. Interface Engineering of Highly Efficient Perovskite Solar Cells. *Science* **2014**, *345*, 542−546.

(10) Jeon, N. J.; Noh, J. H.; Kim, Y. C.; Yang, W. S.; Ryu, S.; Seok, S. I. Solvent Engineering for High-Performance Inorganic−Organic Hybrid Perovskite Solar Cells. *Nat. Mater.* **2014**, *13*, 897−903.

(11) Yang, W. S.; Noh, J. H.; Jeon, N. J.; Kim, Y. C.; Ryu, S.; Seo, J.; Seok, S. I. High-Performance Photovoltaic Perovskite Layers Fabricated through Intramolecular Exchange. *Science* **2015**, *348*, 1234−1237.

(12) Zhu, H.; Fu, Y.; Meng, F.; Wu, X.; Gong, Z.; Ding, Q.; Gustafsson, M. V.; Trinh, M. T.; Jin, S.; Zhu, X. Lead Halide Perovskite Nanowire Lasers with Low Lasing Thresholds and High Quality Factors. *Nat. Mater.* **2015**, *14*, 636−642.

(13) Frost, J. M.; Butler, K. T.; Brivio, F.; Hendon, C. H.; Van Schilfgaarde, M.; Walsh, A. Atomistic Origins of High-Performance in Hybrid Halide Perovskite Solar Cells. *Nano Lett.* **2014**, *14*, 2584−2590.

(14) Liu, S.; Zheng, F.; Koocher, N. Z.; Takenaka, H.; Wang, F.; Rappe, A. M. Ferroelectric Domain Wall Induced Band Gap Reduction and Charge Separation in Organometal Halide Perovskites. *J. Phys. Chem. Lett.* **2015**, *6*, 693−699.

(15) Ma, J.; Wang, L.-W. Nanoscale Charge Localization Induced by Random Orientations of Organic Molecules in Hybrid Perovskite $CH_3NH_3PbI_3$. *Nano Lett.* **2015**, *15*, 248−253.

(16) Kim, Y.-J.; Dang, T.-V.; Choi, H.-J.; Park, B.-J.; Eom, J.-H.; Song, H.-A.; Seol, D.; Kim, Y.; Shin, S.-H.; Nah, J.; et al. Piezoelectric Properties of $CH_3NH_3PbI_3$ Perovskite Thin Films and Their Applications in Piezoelectric Generators. *J. Mater. Chem. A* **2016**, *4*, 756−763.

(17) Ding, R.; Liu, H.; Zhang, X.; Xiao, J.; Kishor, R.; Sun, H.; Zhu, B.; Chen, G.; Gao, F.; Feng, X.; et al. Flexible Piezoelectric Nanocomposite Generators Based on Formamidinium Lead Halide Perovskite Nanoparticles. *Adv. Funct. Mater.* **2016**, *26*, 7708−7716.

(18) Ding, R.; Zhang, X.; Chen, G.; Wang, H.; Kishor, R.; Xiao, J.; Gao, F.; Zeng, K.; Chen, X.; Sun, X. W.; et al. High-Performance Piezoelectric Nanogenerators Composed of Formamidinium Lead Halide Perovskite Nanoparticles and Poly (Vinylidene Fluoride). *Nano Energy* **2017**, *37*, 126−135.

(19) Khan, A. A.; Huang, G.; Rana, M. M.; Mei, N.; Biondi, M.; Rassel, S.; Tanguy, N.; Sun, B.; Leonenko, Z.; Yan, N.; et al. Superior Transverse Piezoelectricity in Organic-Inorganic Hybrid Perovskite Nanorods for Mechanical Energy Harvesting. *Nano Energy* **2021**, *86*, No. 106039.

(20) Sultana, A.; Sadhukhan, P.; Alam, M. M.; Das, S.; Middya, T. R.; Mandal, D. Organo-Lead Halide Perovskite Induced Electroactive B-Phase in Porous PVDF Films: An Excellent Material for Photoactive Piezoelectric Energy Harvester and Photodetector. *ACS Appl. Mater. Interfaces* **2018**, *10*, 4121−4130.
(21) Noh, J. H.; Im, S. H.; Heo, J. H.; Mandal, T. N.; Seok, S. I. Chemical Management for Colorful, Efficient, and Stable Inorganic−Organic Hybrid Nanostructured Solar Cells. *Nano Lett.* **2013**, *13*, 1764−1769.
(22) Kim, D. B.; Park, K. H.; Cho, Y. S. Origin of High Piezoelectricity of Inorganic Halide Perovskite Thin Films and Their Electro-mechanical Energy-Harvesting and Physiological Current-Sensing Characteristics. *Energy Environ. Sci.* **2020**, *13*, 2077−2086.
(23) Chen, H.; Zhou, L.; Fang, Z.; Wang, S.; Yang, T.; Zhu, L.; Hou, X.; Wang, H.; Wang, Z. L. Piezoelectric Nanogenerator Based on in Situ Growth All-Inorganic $CsPbBr_3$ Perovskite Nanocrystals in Pvdf Fibers with Long-Term Stability. *Adv. Funct. Mater.* **2021**, *31*, No. 2011073.
(24) Lee, Y. H.; Shabbir, I.; Yoo, K. H.; Kim, T. W. Significant Enhancement of Output Performance of Piezoelectric Nanogenerators Based on $CsPbBr_3$ Quantum Dots-NOA63 Nanocomposites. *Nano Energy* **2021**, *85*, No. 105975.
(25) Mondal, S.; Paul, T.; Maiti, S.; Das, B. K.; Chattopadhyay, K. K. Human Motion Interactive Mechanical Energy Harvester Based on All Inorganic Perovskite-PVDF. *Nano Energy* **2020**, *74*, No. 104870.
(26) Eperon, G. E.; Paternò, G. M.; Sutton, R. J.; Zampetti, A.; Haghighirad, A. A.; Cacialli, F.; Snaith, H. J. Inorganic Caesium Lead Iodide Perovskite Solar Cells. *J. Mater. Chem. A* **2015**, *3*, 19688−19695.
(27) Choi, H.; Jeong, J.; Kim, H.-B.; Kim, S.; Walker, B.; Kim, G.-H.; Kim, J. Y. Cesium-Doped Methylammonium Lead Iodide Perovskite Light Absorber for Hybrid Solar Cells. *Nano Energy* **2014**, *7*, 80−85.
(28) Straus, D. B.; Guo, S.; Cava, R. J. Kinetically Stable Single Crystals of Perovskite-Phase $CsPbBr_3$. *J. Am. Chem. Soc.* **2019**, *141*, 11435−11439.
(29) Li, B.; Zhang, Y.; Fu, L.; Yu, T.; Zhou, S.; Zhang, L.; Yin, L. Surface Passivation Engineering Strategy to Fully-Inorganic Cubic $CsPbI_3$ Perovskites for High-Performance Solar Cells. *Nat. Commun.* **2018**, *9*, No. 1076.
(30) Jeong, B.; Han, H.; Kim, H. H.; Choi, W. K.; Park, Y. J.; Park, C. Polymer-Assisted Nanoimprinting for Environment-and Phase-Stable Perovskite Nanopatterns. *ACS Nano* **2020**, *14*, 1645−1655.
(31) Luo, P.; Xia, W.; Zhou, S.; Sun, L.; Cheng, J.; Xu, C.; Lu, Y. Solvent Engineering for Ambient-Air-Processed, Phase-Stable $CsPbI_3$ in Perovskite Solar Cells. *J. Phys. Chem. Lett.* **2016**, *7*, 3603−3608.
(32) Wang, Y.; Dar, M. I.; Ono, L. K.; Zhang, T.; Kan, M.; Li, Y.; Zhang, L.; Wang, X.; Yang, Y.; Gao, X.; et al. Thermodynamically Stabilized Beta-$CsPbI_3$−Based Perovskite Solar Cells with Efficiencies >18%. *Science* **2019**, *365*, 591−595.
(33) Shepelin, N. A.; Glushenkov, A. M.; Lussini, V. C.; Fox, P. J.; Dicinoski, G. W.; Shapter, J. G.; Ellis, A. V. New Developments in Composites, Copolymer Technologies and Processing Techniques for Flexible Fluoropolymer Piezoelectric Generators for Efficient Energy Harvesting. *Energy Environ. Sci.* **2019**, *12*, 1143−1176.
(34) Railsback, L. B. Some Fundamentals of Mineralogy and Geochemistry, 2006. www.gly.uga.edu/railsback.
(35) Maity, K.; Pal, U.; Mishra, H. K.; Maji, P.; Sadhukhan, P.; Mallick, Z.; Das, S.; Mondal, B.; Mandal, D. Piezo-Phototronic Effect in Highly Stable $CsPbI_3$-PDVF Composite for Self-Powered Nanogenerator and Photodetector. *Nano Energy* **2022**, *92*, No. 106743.
(36) Li, J.; Meng, Q.; Li, W.; Zhang, Z. Influence of Crystalline Properties on the Dielectric and Energy Storage Properties of Poly (Vinylidene Fluoride). *J. Appl. Polym. Sci.* **2011**, *122*, 1659−1668.
(37) Agronin, A. G.; Rosenwaks, Y.; Rosenman, G. I. Piezoelectric Coefficient Measurements in Ferroelectric Single Crystals Using High Voltage Atomic Force Microscopy. *Nano Lett.* **2003**, *3*, 169−171.
(38) Deng, Z.; Dai, Y.; Chen, W.; Pei, X.; Liao, J. Synthesis and Characterization of Bowl-Like Single-Crystalline $BaTiO_3$ Nano-particles. *Nanoscale Res. Lett.* **2010**, *5*, 1217−1221.
(39) Yadav, S. K.; Mahapatra, S. S.; Cho, J. W.; Lee, J. Y. Functionalization of Multiwalled Carbon Nanotubes with Poly (Styrene-B-(Ethylene-Co-Butylene)-B-Styrene) by Click Coupling. *J. Phys. Chem. C* **2010**, *114*, 11395−11400.
(40) Huang, C.; Zhang, Q. M. Fully Functionalized High-Dielectric-Constant Nanophase Polymers with High Electromechanical Response. *Adv. Mater.* **2005**, *17*, 1153−1158.
(41) Jella, V.; Ippili, S.; Eom, J.-H.; Choi, J.; Yoon, S.-G. Enhanced Output Performance of a Flexible Piezoelectric Energy Harvester Based on Stable $MAPbI_3$-PVDF Composite Films. *Nano Energy* **2018**, *53*, 46−56.
(42) Rao, Y.; McEachern, K. M.; Arnold, D. P. A Compact Human-Powered Energy Harvesting System. *J. Phys.: Conf. Ser.* **2013**, *476*, No. 012011.
(43) Zhou, L.; Yang, T.; Zhu, L.; Li, W.; Wang, S.; Hou, X.; Mao, X.; Wang, Z. L. Piezoelectric Nanogenerators with High Performance against Harsh Conditions Based on Tunable N Doped 4H-SiC Nanowire Arrays. *Nano Energy* **2021**, *83*, No. 105826.
(44) Huang, G.; Khan, A. A.; Rana, M. M.; Xu, C.; Xu, S.; Saritas, R.; Zhang, S.; Abdel-Rahmand, E.; Turban, P.; Ababou-Girard, S.; et al. Achieving Ultrahigh Piezoelectricity in Organic−Inorganic Vacancy-Ordered Halide Double Perovskites for Mechanical Energy Harvesting. *ACS Energy Lett.* **2021**, *6*, 16−23.
(45) Rana, M. M.; Khan, A. A.; Huang, G.; Mei, N.; Saritas, R.; Wen, B.; Zhang, S.; Voss, P.; Abdel-Rahman, E.; Leonenko, Z.; et al. Porosity Modulated High-Performance Piezoelectric Nanogenerator Based on Organic/Inorganic Nanomaterials for Self-Powered Structural Health Monitoring. *ACS Appl. Mater. Interfaces* **2020**, *12*, 47503−47512.

https://doi.org/10.1021/acsomega.2c00091
ACS Omega 2022, 7, 10559−10567